

Ultrafast optoelectronic processes in 1D radial van der Waals heterostructures: carbon, boron nitride and MoS₂ nanotubes with coexisting excitons and highly mobile charges

Maria G. Burdanova,[†] Reza J. Kashtiban,[†] Yongjia Zheng,[‡] Rong Xiang,[‡] Shohei Chiashi,[‡] Jack Matthew Woolley,[¶] Michael Staniforth,[¶] Emily Sakamoto-Rablah,[†] Xue Xie,[†] Matthew Broome,[†] Jeremy Sloan,[†] Anton Anisimov,[§] Esko I. Kauppinen,^{||} Shigeo Maruyama,[‡] and James Lloyd-Hughes^{*,†}

[†]*University of Warwick, Department of Physics, Gibbet Hill Road, Coventry, CV4 7AL, United Kingdom.*

[‡]*Department of Mechanical Engineering, The University of Tokyo, Tokyo 113-8656, Japan.*

[¶]*University of Warwick, Department of Chemistry, Gibbet Hill Road, Coventry, CV4 7AL, United Kingdom.*

[§]*Canatu Ltd., Helsinki FI00390, Finland.*

^{||}*Department of Applied Physics, Aalto University School of Science, Espoo 15100, FI-00076 Aalto, Finland.*

E-mail: j.lloyd-hughes@warwick.ac.uk

Abstract

Heterostructures built from 2D, atomically-thin crystals are bound by the van der Waals force, and exhibit unique optoelectronic properties. Here, we report the struc-

ture, composition and optoelectronic properties of 1D van der Waals heterostructures comprising carbon nanotubes wrapped by atomically-thin nanotubes of boron nitride and molybdenum disulfide (MoS₂). The high quality of the composite was directly evidenced on the atomic scale by transmission electron microscopy, and on the macroscopic scale by a study of the heterostructure's equilibrium and ultrafast optoelectronics. Ultrafast pump-probe spectroscopy across the visible and terahertz frequency ranges identified that, in the MoS₂ nanotubes, excitons coexisted with a prominent population of free charges. The electron mobility was comparable to that found in high-quality atomically-thin crystals. The high mobility of the MoS₂ nanotubes highlights the potential of 1D van der Waals heterostructures for nanoscale optoelectronic devices.

Keywords

nanotubes; van der Waals heterostructures; ultrafast; terahertz

Atomically thin crystals and their heterostructures are creating entirely new paradigms in the design of advanced optoelectronic materials. Novel 2D materials, as exemplified by the transition metal dichalcogenides (TMDs), feature exotic properties such as strong Coulomb interactions, efficient luminescence and spin-valley physics.¹⁻⁵ Significant exciton binding energies E_B arise from the weak, non-local dielectric screening of the Coulomb interaction in 2D atomically-thin TMDs, combined with the relatively high effective masses of carriers:⁵ for instance $E_B = 0.24 - 0.27$ eV for the A exciton in a MoS₂ monolayer.^{6,7}

Heterostructures of atomically thin 2D materials show unique emergent properties associated with interlayer coupling and charge transfer, opening up new possibilities for the development of nanoelectronic devices.^{8,9} In such van der Waals (vdW) heterostructures, excitons can remain tightly bound even across lateral and vertical heterojunctions. While the study of 2D heterostructures has undergone rapid growth, 1D vdW heterostructures¹⁰ in a wire geometry offer unique nano-optoelectronic applications including field effect tran-

sistors, where inner carbon nanotubes (CNTs) are used to electrically gate an outer TMD nanotube, such as MoS₂,¹⁰ or radial p-n junctions for nano-scale photovoltaics or photodetectors,¹¹ for instance exploiting flexoelectricity.¹² When 2D materials roll up to form 1D nanotubes, dramatic changes in the optoelectronic properties result from curvature and quantum confinement, as exemplified by the comparison between graphene, a Dirac semi-metal with no excitons, and semiconducting carbon nanotubes, which host excitons. Hence it is of fundamental and applied interest to explore the nature of quasiparticles created after photoexcitation of 1D vdW heterostructures that include TMDs.

Here we report the equilibrium and dynamic optoelectronic properties of a 1D vdW heterostructure consisting of bundles of carbon nanotubes wrapped by boron nitride nanotubes (BNNTs) and molybdenum disulphide nanotubes (MoS₂ NTs). Chemical vapour deposition created radial heterostructures, using free-standing films of carbon nanotubes as the initial template.¹⁰ The BN overgrowth served to wrap each CNT bundle, creating a template with sufficient diameter (>5 nm) for the subsequent deposition of atomically-thin MoS₂. For narrower diameters the high strain energy of MoS₂ prohibited nanotube growth.¹⁰ The unique excitonic, vibrational and conductive properties of each layer were disentangled for the composite (denoted C@BN@MoS₂) by reference to the pristine CNT template and a radial heterostructure of CNTs wrapped only by BN (denoted C@BN).

The composition and morphology of the 1D vdW heterostructures were directly imaged using scanning transmission electron microscopy (STEM). Low magnification annular dark-field (ADF) STEM images (Fig. 1a and 1b) and scanning electron microscopy images (Supplemental Fig. S1) demonstrated high purity, randomly oriented nanowires. Brighter regions in the dark-field STEM images result from areas with higher atomic number: hence the nanowires in Fig. 1a indicate predominantly the Mo atoms, while the nanowires in Fig. 1b show the extent of the BNNTs. These images directly attest to the high coverage of MoS₂ NTs on the BNNT templates. Measurements on the CNT template film established the 2.1 nm diameter CNTs form bundles with mean diameter 7.9 nm. After BN overgrowth

the mean nanowire diameter was 11.1 nm (average 4-5 walls of BN), rising to 14.1 nm after MoS₂ growth (2-3 walls) [Supplemental Fig. S2].

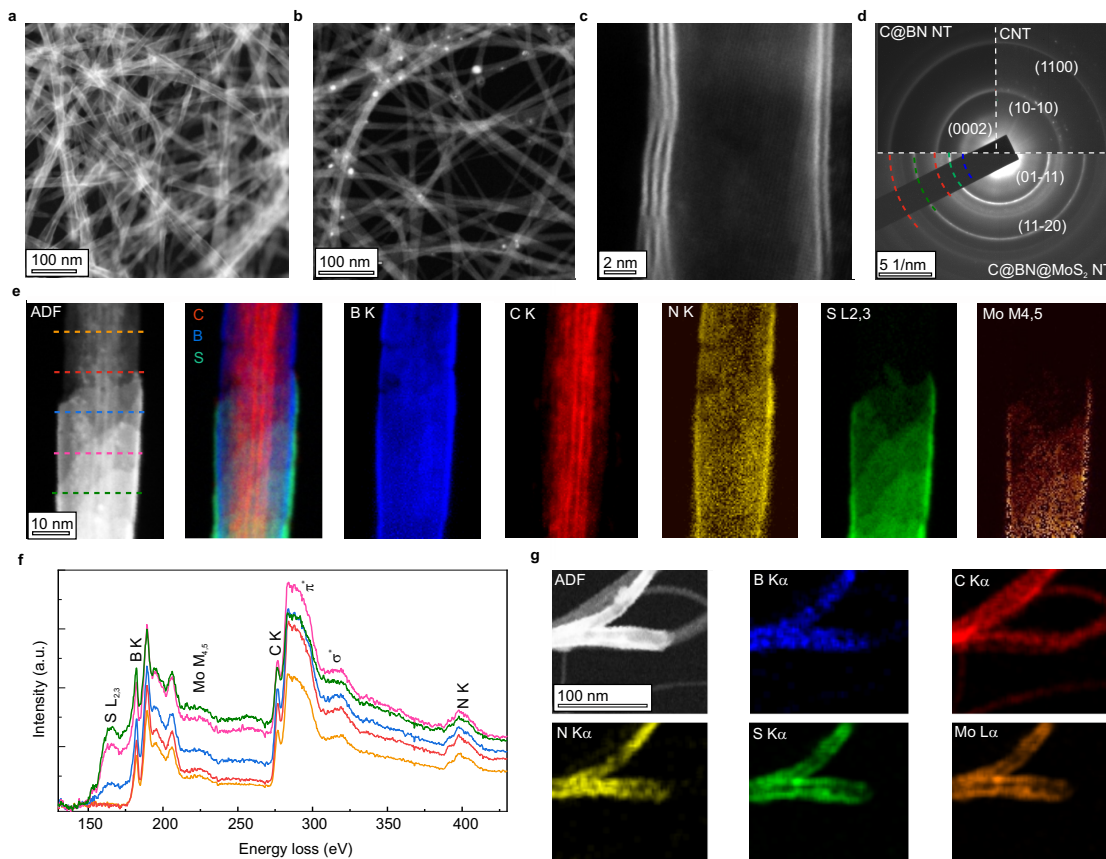


Figure 1: Structure and composition of 1D vdW heterostructure. ADF-STEM images of C@BN@MoS₂ NT (a) and C@BN NT (b) heterostructure films. (c) ADF image of multi-walled MoS₂ tube. (d) Selected-area electron diffraction obtained over a 3.5 μm^2 area for CNT (top-right), C@BN NT (top-left) and C@BN@MoS₂ NT (bottom) films. (e) ADF image of C@BN@MoS₂ NTs near the end of a MoS₂ NT, and the corresponding EELS elemental maps. From top to bottom an increase from zero to three MoS₂ walls can be observed, most clearly using the S L edge. (f) EELS spectra integrated along the five lines shown in (e); (g) ADF image of C@BN@MoS₂ NT heterostructure near the end of a MoS₂ NT, and the corresponding EDX elemental maps.

The typical wall thickness of the MoS₂ NTs was directly confirmed by ADF-STEM images: Fig. 1c shows a 1D vdW heterostructure with two MoS₂ walls (right) and three walls (left) indicating partial wrapping by a third MoS₂ nanotube. Selected-area electron diffraction patterns (Fig. 1d) showed diffraction rings consistent with randomly-oriented nanotubes

and the lattice constants of CNTs, multi-layer hexagonal BN (hBN) and MoS₂. STEM electron energy loss spectroscopy (EELS near the end of an incomplete MoS₂ NT (Fig. 1e, f) and energy-dispersive X-ray spectroscopy (Fig. 1g) verified that the 1D heterostructure contained bundles of CNTs (red) covered by multi-walled BNNTs and MoS₂ NTs.

Each additional layer in a 1D vdW heterostructure may alter the optoelectronic properties of the final composite, either by detrimental changes to the encapsulated layers during overgrowth, or by interlayer charge or energy transfer. We assessed sample quality by comparing the equilibrium optical absorbance, A_0 , for the pristine CNT film with that after each overgrowth. The C@BN@MoS₂ NT film exhibited an optical absorbance (Fig. 2a, green line) arising from the combination of the absorbance of atomically-thin crystalline MoS₂, BN and C nanotubes, demonstrating that the growth process did not degrade the optoelectronic properties of the filling.

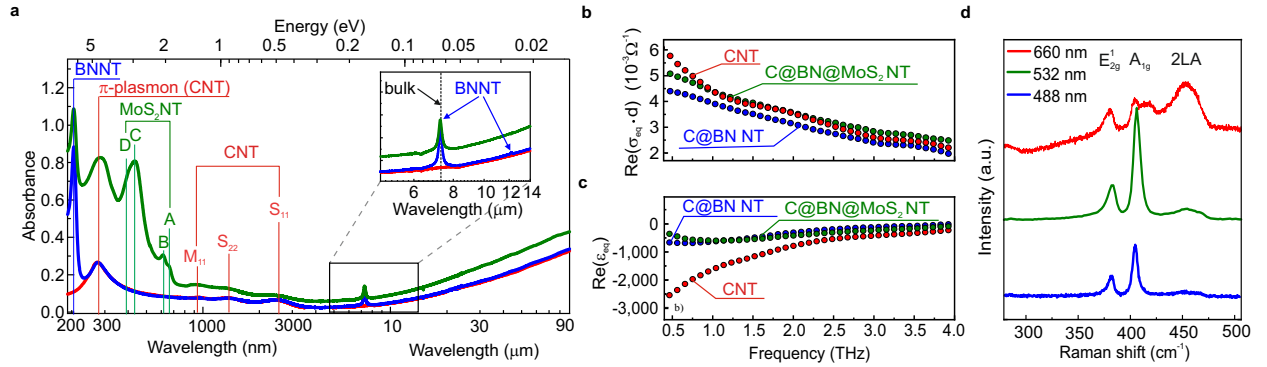


Figure 2: Optical and vibrational properties of C, C@BN and C@BN@MoS₂ NTs. (a) UV-visible-IR absorbance $A_0 = 10^{-T}$ for C (red), C@BN (blue) and C@BN@MoS₂ (green) NT films. Near-infrared excitonic absorption peaks associated with semiconducting (S₁₁ and S₂₂) and metallic (M₁₁) SWCNTs are evident at 2300 nm, 1300 nm and 890 nm respectively. The sharp absorption at 205 nm (6.0 eV) is from the exciton in BN. The inset shows the in-plane stretch (1378 cm⁻¹) and out-of-plane radial buckling (823 cm⁻¹) modes associated with BN. The dashed black vertical line corresponds to the in-plane stretch mode of bulk h-BN (1367 cm⁻¹).¹³ (b) Real part of equilibrium conductivity of C (red circles), C@BN (blue circles) and C@BN@MoS₂ (green circles) NT films. (c) As (b), for the real part of the dielectric function in equilibrium. (d) Raman spectra of C@BN@MoS₂ NTs under 488 nm (blue), 532 nm (red) and 660 nm (green) laser excitation.

The absorption spectra of the C@BN@MoS₂ NTs show features associated with the ex-

citonic and interband absorption of MoS₂, such as the A (660 nm, 1.88 eV) and B (613 nm, 2.02 eV) excitons, and the C (435 nm, 2.85 eV) and D (400 nm, 3.10 eV) interband transitions of MoS₂,^{14,15} similar to atomically-thin MoS₂.¹⁶ The A and B peaks in MoS₂ are associated with *K*-point excitons separated by the spin-orbit splitting energy of the valence band. For monolayer MoS₂ the conduction band (CB) minimum and valence band (VB) maximum coincide at the *K* point, with a single-particle direct bandgap of 2.1 eV.¹⁷ For bilayer and thicker MoS₂, the optical absorption at *K* is similar, but a rise in the valence band maximum at Γ , and a drop in the conduction band minimum at *Q*, creates an indirect gap material.^{5,17}

Despite the strong absorption of the C@BN@MoS₂ film (around 4 times that of monolayer MoS₂¹⁸), no photoluminescence was observed for the 1D MoS₂ NTs, whereas under the same conditions a reference monolayer of 2D MoS₂ showed photoluminescence at the A exciton (Supplemental Fig. S3). This suggests that the MoS₂ nanotubes (2-3 monolayers) have an indirect bandgap, similar to bilayer and thicker 2D MoS₂. Armchair, zigzag and chiral MoS₂ NTs were calculated to have similar optical absorption spectra,¹⁹ particularly in the large diameter limit, with strong absorption above 2 eV similar to that observed here.

To elucidate intraband carrier motion in the 1D vdW heterostructures, the real parts of the effective THz conductivity in equilibrium, $\text{Re}(\sigma_{\text{eq}})$ and the real parts of the effective dielectric function, $\text{Re}(\epsilon_{\text{eq}})$, are reported in Fig. 2(b) (see Fig. S4 for $\text{Im}(\sigma_{\text{eq}})$). Here, the “effective” optical properties are averages over the composite, rather than representing local, microscopic response functions. The role of each layer is highlighted by the subtle changes evident between the reference C, C@BN and C@BN@MoS₂ NT films. The rise in $\text{Re}(\sigma_{\text{eq}})$ towards lower frequency (higher wavelength) for the CNT film is consistent with previous studies of CNT films with a similar morphology, where the THz conductivity contains a contribution from Drude-like free-carrier absorption and from axial plasmons.^{20–22} The C@BN NTs retain a large fraction of the conductivity of the CNTs (> 90% at 1 THz), demonstrating that the inner CNTs in the heterostructure are highly conductive, and may be used to electrically gate the outer layers in future devices. The addition of the 4-5 insulating layers

of BN reduces $\text{Re}(\sigma_{\text{eq}})$ and lowers the negative $\text{Re}(\epsilon_{\text{eq}})$ characteristic of a highly conductive material. This suppression is most prominent at low frequencies, suggesting a lower dc conductivity. BN acts as a good tunnel barrier even for a monolayer,²³ and hence reduces intertube conductivity, while the intratube (plasmonic) conductivity remains comparable.

The addition of the MoS₂ NTs in the C@BN@MoS₂ composite creates a small increase in $\text{Re}(\sigma_{\text{eq}})$ across the THz range in comparison to the C@BN NTs. This extra conductivity may be associated with free charges in the outer MoS₂ NT if the as-grown material is doped: indeed MoS₂ monolayers are often n-doped as a result of S-vacancies.²⁴ Alternatively, the MoS₂ NTs may have altered the conductivity of the encapsulated CNTs, either as a result of a strain-induced change in their bandstructure, or by a small but finite charge transfer from the outer MoS₂ NTs to the inner CNTs (possible given the estimated band alignment, Supplemental Fig. S5).

The C@BN and C@BN@MoS₂ NTs have distinct electronic and vibrational resonances that can be further investigated by Raman spectroscopy. The out-of-plane and in-plane Raman active phonons have been widely used to distinguish monolayer MoS₂ from bilayer and thicker structures, based on their position and splitting.^{25,26} For the C@BN@MoS₂ NT film the in-plane E_{2g}^1 and out-of-plane A_{1g} mode [Fig. 2 (d)], are in agreement with theoretical predictions for MoS₂ NTs.^{27,28} Raman spectra taken for different laser wavelengths highlight the longitudinal acoustic (2LA) modes at 460 and 470 cm⁻¹: these second-order Raman features are associated with intervalley electron transitions created by two LA phonons close to the K or M points, and which are relatively intense for resonant excitation of the A and B excitons,²⁹ as is evident here under excitation at 660 nm (resonant to the A exciton). A weak feature at ~ 420 cm⁻¹ under 660 nm excitation is associated with a combination of LA and transverse acoustic (TA) phonon modes around the K point, due to a doubly-resonant intervalley electron scattering process.³⁰ The Raman results indicate that excitons in 1D MoS₂ nanotubes may undergo rapid intervalley charge transfer, as reported for 2D MoS₂.³⁰

To establish whether excitons in the MoS₂ nanotubes are the principle photoproduct

after light is absorbed by the MoS₂ component of the vdW heterostructure, we tracked the dynamical absorbance in the UV and visible range at different pump-probe delay times t after femtosecond pulsed excitation. In Fig. 3 broadband transient absorption spectra of the C@BN@MoS₂ NTs are shown for excitation at 350 nm (at energies above the D peak). The pump was absorbed predominantly in the MoS₂ NTs, which had high absorbance compared to the C and BN NTs (Fig.2a) at this pump wavelength. The probe wavelengths (315-720 nm) covered the absorption range of the MoS₂ NTs, and were higher in energy than the S_{11} , S_{22} and M_{11} energies where CNTs exhibit their transient response.³¹

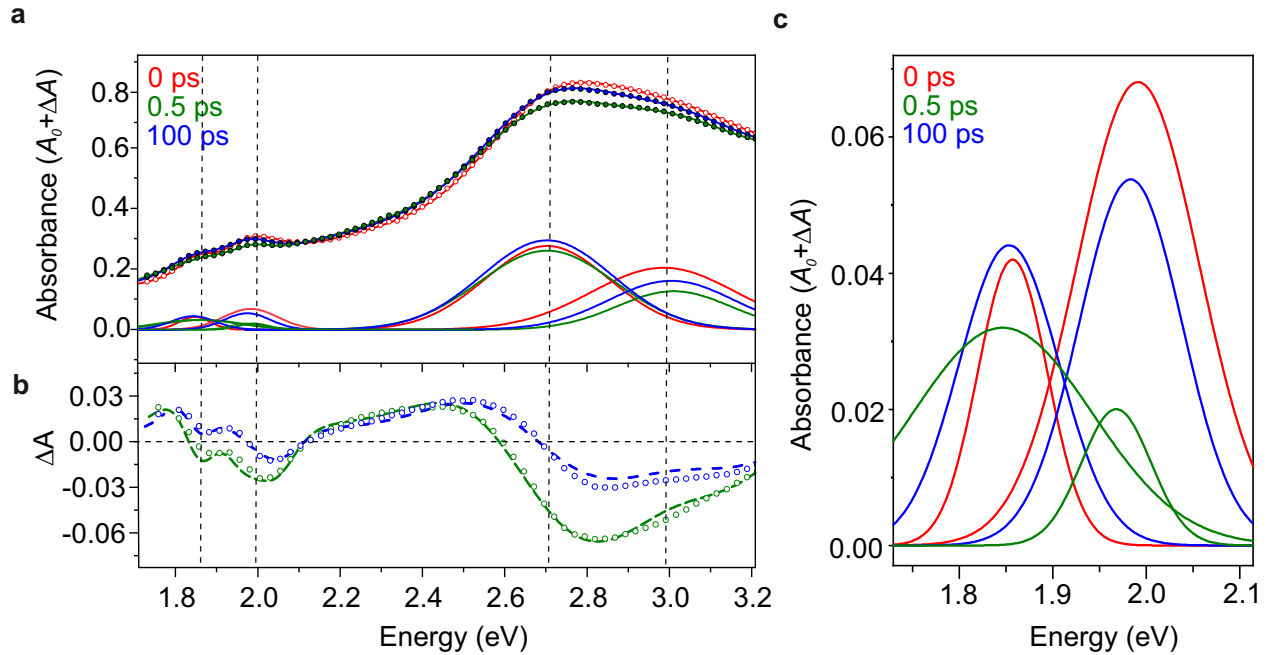


Figure 3: Transient absorption spectroscopy of C@BN@MoS₂ NT film. (a) Transient absorption spectra, $A(E, t) = A_0(E) + \Delta A(E, t)$, as a function of pump-probe delay time t and probe beam energy E (excitation wavelength 350 nm; 1 mJcm^{-2} fluence). Here, $t = 0.0 \text{ ps}$ was defined as the probe pulse arriving just before the pump pulse, and hence shows the equilibrium absorbance, $A_0(E)$, (empty red circles). Data at $t = 0.5 \text{ ps}$ (green circles) and $t = 100 \text{ ps}$ (blue circles) are also shown, along with fits (solid lines). The dashed vertical lines correspond (from left to right) to the A, B, C and D features in the equilibrium absorbance, while the contribution from each peak is shown by the lower colored lines. (b) $\Delta A(E, t)$ spectra from experiment (circles) and corresponding fits (dashed lines) at $t = 0.5 \text{ ps}$ (green) and $t = 100 \text{ ps}$ (blue). (c) Expanded view of the fitted absorbance in the range near the A and B excitons, with the same color code as in (a).

The total absorbance spectra $A(E, t) = A_0(E) + \Delta A(E, t)$ are reported in Fig. 3(a), where $t = 0$ (red dashed line) corresponds to the probe arriving immediately prior to the pump, and thus shows the absorbance in equilibrium around the A, B, C and D peaks (dashed vertical lines). We modelled the experimental absorbance at each pump-probe delay using 4 resonances with variable energy, linewidth and strength (lower curves in Fig. 3(a)) superimposed on top of a monotonically increasing background accounting for the absorbance of the CNTs. The fitted ΔA (Fig. 3(b), dashed lines) reproduced the experimental data (points). The contributions from the A and B excitons to the fitted absorbance is reported in Figure 3(c).

Prominent A and B excitonic absorption was present at all time delays, and at similar energies to equilibrium. From this we can conclude that, similar to the case of monolayer 2D MoS₂ and other TMDs, excitons are the primary photoproduct in the MoS₂ layers of the present vdW heterostructure. Further, the exciton dynamics are similar to those reported in monolayer MoS₂,¹⁸ suggesting that there was no substantial charge transfer to the CNT. Modifications to the strength and linewidth of the A and B excitons account for the observed ΔA in the 1.7-2.2 eV range. Immediately after photoexcitation, the B exciton lowered in strength, but retained a similar linewidth to that in equilibrium [Figure 3(c)]. The A exciton broadened, and increased in strength above its equilibrium level after 1 ps, creating a positive ΔA at energies below 1.98 eV (Supplemental Fig. S6). Similar trends were observed at all pump wavelengths, including resonant to the A exciton. Changes in the interband absorption strength (2.2-3.2 eV), including around the C and D peaks, were also evident, and can be linked to bandgap renormalization.^{18,32}

The broader A-exciton linewidth results from faster energy, phase or momentum relaxation after photoexcitation, as in atomically-thin 2D TMDs.⁵ However, the increase in A exciton strength here is unusual and may result from either the dynamic screening of the Coulomb interaction, or from trion formation. In the former case, the finite quasiparticle density screens the Coulomb interaction, lowering the binding energy and redshifting the

single-particle bandgap, with little change in the excitons' energies.⁵ A weaker Coulomb interaction reduces the exciton oscillator strength, consistent with the B exciton's lower absorbance after photoexcitation, but inconsistent with the A exciton's increased strength. Alternatively, if the MoS₂ NTs are lightly doped in equilibrium (as suggested by the THz conductivity spectra above), the A exciton's absorption strength is partially reduced by Pauli blocking, similarly to the case for doped CNTs.²² When the pump pulse injects excitons, the formation of trions removes the extrinsic charges from the conduction band or valence band, thereby removing the Pauli blocking effect and increasing the A exciton's absorbance, consistent with the experimental result.

To utilise 1D vdW heterostructures in nanoelectronic devices (e.g. photovoltaics) free charges may be desirable rather than excitons. Optical pump-THz probe (OPTP) spectroscopy allows the presence of free, unbound charges in semiconductor nanomaterials to be uniquely established.^{33,34} While some studies of the THz photo-response of MoS₂ monolayers have reported positive photoconductivity linked to free carriers in an electron-hole plasma,³⁵ other studies reported negative photoconductivity assigned to trion formation,³⁶ in particular for n-doped monolayers.³⁷

The dynamical THz photoconductivity of the 1D vdW heterostructures is reported in Figures 4 and 5. The magnitude and dynamic of the THz differential transmission $\Delta T/T$ [Fig. 4(a)] was similar for the CNT and C@BN NT samples: as shown in Figure 2 BN did not absorb photons at the pump wavelengths used (340-950 nm), and BN encapsulation did not radically alter the optoelectronic properties of the CNTs. The C@BN@MoS₂ film exhibited a different dynamic [Fig. 4(a)], crossing from $\Delta T/T > 0$ at early times to $\Delta T/T < 0$ for $t > 7$ ps. For pump wavelengths from 350 nm to 650 nm, corresponding to strong absorption of the pump in the MoS₂ NTs, this cross-over in $\Delta T/T$ was universally observed [Fig. 4(b)]. However it was not seen at longer pump wavelengths (950 nm), when only the CNTs absorbed the pump.

This complex dynamic can be understood with reference to Figure 5. At early times, the

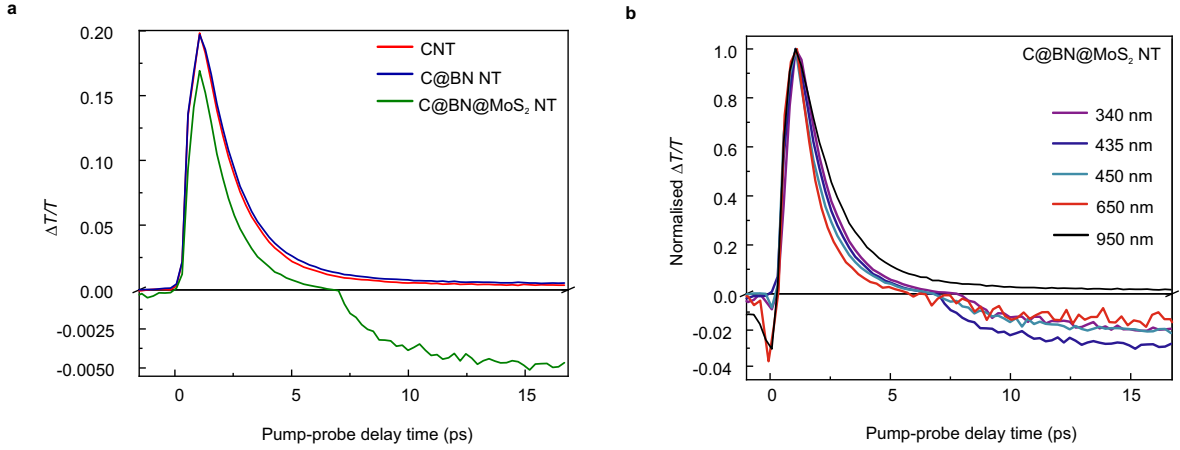


Figure 4: Transient THz response of CNT, C@BN NT, C@BN@MoS₂ NT (a) at 435 nm pump wavelength with $100 \mu\text{Jcm}^{-2}$ fluence, (b) at 340 nm, 435 nm, 450 nm, 650 nm and 950 nm.

strong positive $\Delta T/T$ for all samples can be attributed to optical excitation of the CNTs, which creates significant negative photoconductivity.²² In equilibrium the CNTs are conductive, as a result of the metallic NTs and doped semiconducting NTs, with a conductivity similar to the Drude model of free-carrier absorption (black line, Fig. 5(a) inset). Optical excitation lowers the carrier density of free charges, n , or increases their effective masses, m^* .²² A simultaneous narrowing of the conductivity spectrum results from a drop in the momentum scattering rate, γ ,²² yielding a conductivity (blue line) lower than that in equilibrium, i.e. negative photoconductivity. At $t = 2$ ps the real and imaginary parts of the experimental photoconductance, $\Delta\sigma(\omega)d$ [points, Fig. 5(b)] were modelled by the Drude function $\Delta\sigma(\omega)d = \sigma_D/(1 - i\omega\tau)$ [solid lines]. Here, the momentum scattering time was $\tau = 1/\gamma = 110$ fs, while the dc photoconductance $\sigma_D = -0.6$ mS (where $1 \text{ mS} \equiv 10^{-3} \Omega^{-1}$) was negative to account for the lower conductivity under photoexcitation.

At later times the negative $\Delta T/T$ corresponds to a positive photoconductivity uniquely associated with mobile charges in the MoS₂ NTs, and which persists for ~ 300 ps (Supplemental Fig. S7). An excitonic origin can be ruled out: excitons in MoS₂ yield intraexcitonic transitions in the mid-infrared³⁸ instead of the THz.³⁴

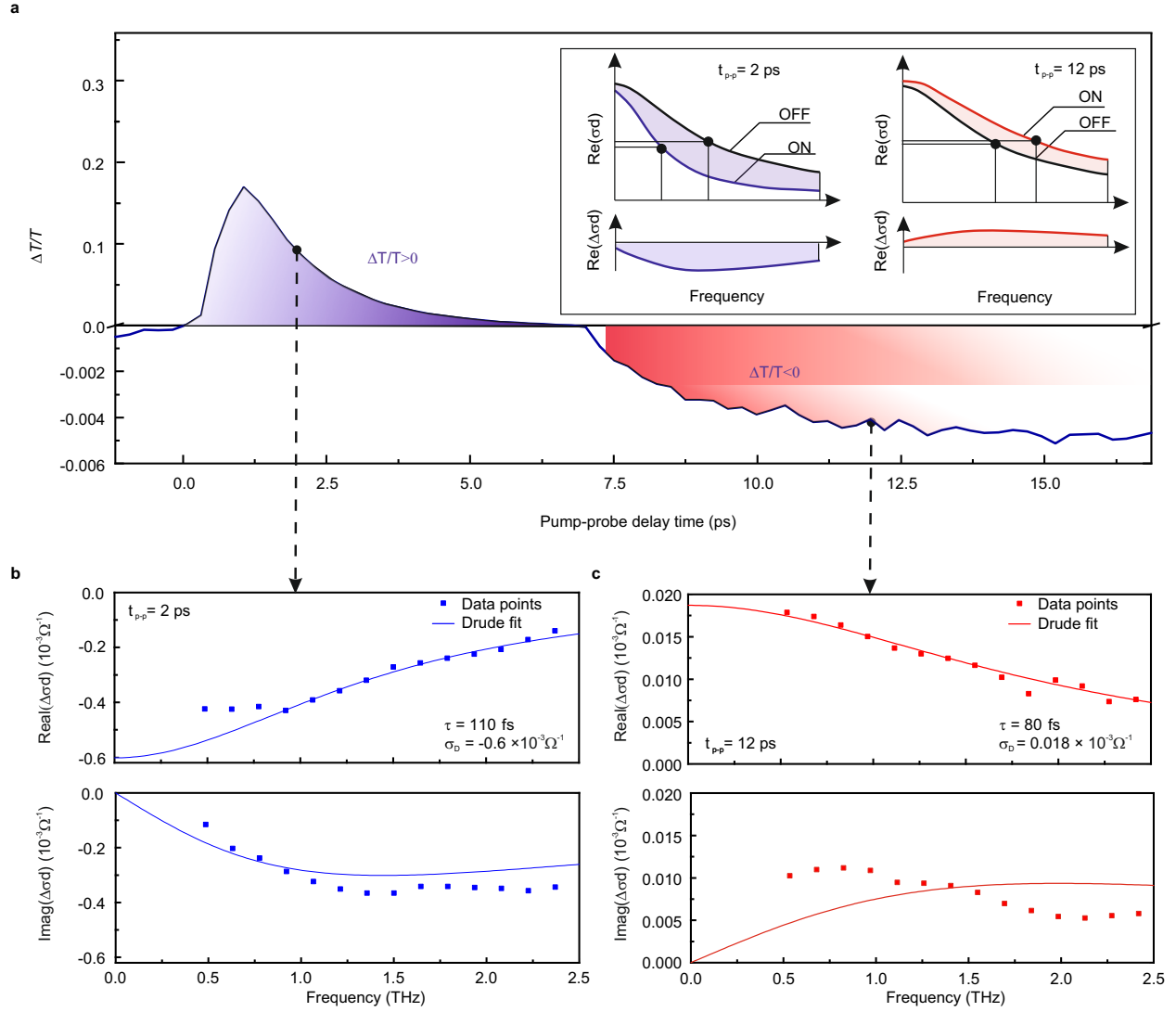


Figure 5: Transient THz response of C@BN@MoS₂ (a) versus pump-probe delay, at 435 nm pump wavelength and $100 \mu\text{Jcm}^{-2}$ fluence. Note the negative and positive y-axes have different scales. The inset shows a schematic of the frequency-dependent conductivity without ('OFF') and with ('ON') photoexcitation, and their difference, $\Delta\sigma(\omega)$. (b) The real and imaginary parts of $\Delta\sigma(\omega)$ at 2 ps (points) show a negative photoconductivity associated with the CNTs, which can be modelled by the Drude model (lines) as described in the text. (c) As in (b), but at 12 ps pump-probe delay, showing the positive photoresponse associated with normal photoconductivity in the MoS₂ NTs.

The real and imaginary parts of the experimental photoconductance at $t = 12$ ps [Fig. 5(d, e)] were modelled as at $t = 2$ ps, but with a positive $\sigma_D = 0.018$ mS and $\tau = 80$ fs, corresponding to $\gamma = 12.5$ THz. Assuming an effective mass $m^* \simeq 0.6m_e$ representative of carriers in the K-valley of MoS₂, the effective mobility of carriers in the MoS₂ NTs is $\mu = e/m^*\gamma \simeq 234$ cm²/Vs. This is comparable to the best field-effect mobilities ($\mu > 200$ cm²/Vs) obtained at room temperature in MoS₂ monolayers³⁹ and multilayered MoS₂.⁴⁰ The THz mobility is a local probe of the intra-NT motion of free charges, and is higher than the mobility derived from transport measurements across multiple nanotubes, where charges cross multiple interfaces. Notably, the mobility observed here for MoS₂ NTs in a 1D vdW heterostructure is higher than the ~ 40 cm²/Vs reported for individual multi-walled MoS₂ nanotubes,⁴¹ and is also higher than reports for monolayer MoS₂ from OPTP spectroscopy.^{37,42} Here, the relatively low momentum scattering rate and significant mobility attests to the high quality and relatively defect-free nature of the MoS₂ NTs.

The observation of free charges in the MoS₂ NTs is intriguing given the prominent excitons, although atomically-thin MoS₂ also exhibits both free charges and excitons.^{43,44} Scenarios for the direct generation of free charges include exciton-exciton annihilation,⁴³ which is most effective at high exciton densities. Here the positive photoconductivity of the MoS₂ NTs was observed to increase linearly over a wide range of pump fluences (10-200 μ Jcm⁻², Supplemental Fig. S8) suggesting that free charges are produced in proportion to the absorbed photon flux. At lower excitation densities, without exciton-exciton annihilation, exciton dissociation can proceed via electron trapping at defects,⁴⁴ leaving mobile holes. Further, the strong 2LA Raman modes resonant to the A-exciton (Figure 2) provide evidence that direct K -point excitons can be scattered into intervalley excitons⁵ consisting of Q -point electrons and K -point holes.⁴⁵

In conclusion, the structure of radial 1D van der Waals heterostructures consisting of carbon nanotubes wrapped by BN and MoS₂ nanotubes was studied on the atomic scale, while the effective optical properties of heterostructure films were examined from UV to

THz wavelengths. A dynamic switch from negative to positive photoconductivity originated from the differing temporal dynamics for free-carrier absorption in the carbon nanotubes and MoS₂ nanotubes. The conductivity of the carbon nanotube cores remained high after BN and MoS₂ fabrication, offering nano-scale electrical devices gated by the carbon nanotubes. Potential applications of these relatively large area ($\sim 1 \text{ cm}^2$) vdW heterostructure films include catalysis or gas sensing, where porous films are advantageous, or in optoelectronic devices requiring wafer-scale areas of high quality TMD semiconductor.

Acknowledgements

The UK authors thank the EPSRC (UK) for support under grant EP/N010825/1 and EP/R019428/1. MGB thanks the Russian Government for financial support (Global Education program). This research received funding from projects 286546 (DEMEC), 292600 (SUPER) and 316572 (CNTstress) supported by the Academy of Finland, as well as projects 3303/31/2015 (CNT-PV) and 1882/31/2016 (FEDOC) supported by BF Finland.

Competing interests

The authors declare no competing interests.

Supporting information

Experimental methods (sample growth; spectroscopic methods) are described in the Supporting Information, which also includes additional electron microscopy and optical spectroscopy results as referenced from the main text. This material is available free of charge via the internet at <http://pubs.acs.org>.

References

1. Mak, K. F.; Lee, C.; Hone, J.; Shan, J.; Heinz, T. F. Atomically Thin MoS₂: A New Direct-Gap Semiconductor. *Phys. Rev. Lett.* **2010**, *105*, 136805.
2. Mak, K.; He, K.; Shan, J.; Heinz, T. Control of valley polarization in monolayer MoS₂ by optical helicity. *Nature Nanotechnology* **2012**, *7*, 494–498.
3. Ye, Z.; Cao, T.; O’Brien, K.; Zhu, H.; Yin, X.; Wang, Y.; Louie, S. G.; Zhang, X. Probing excitonic dark states in single-layer tungsten disulphide. *Nature* **2014**, *513*, 214 – 218.
4. Nagler, P.; Plechinger, G.; Ballottin, M. V.; Mitioglu, A.; Meier, S.; Paradiso, N.; Strunk, C.; Chernikov, A.; Christianen, P. C. M.; Schller, C. *et al.* Interlayer exciton dynamics in a dichalcogenide monolayer heterostructure. *2D Materials* **2017**, *4*, 025112.
5. Wang, G.; Chernikov, A.; Glazov, M. M.; Heinz, T. F.; Marie, X.; Amand, T.; Urbaszek, B. Colloquium: Excitons in atomically thin transition metal dichalcogenides. *Rev. Mod. Phys.* **2018**, *90*, 021001.
6. Park, S.; Mutz, N.; Schultz, T.; Blumstengel, S.; Han, A.; Aljarb, A.; Li, L.-J.; List-Kratochvil, E. J. W.; Amsalem, P.; Koch, N. Direct determination of monolayer MoS₂ and WSe₂ exciton binding energies on insulating and metallic substrates. *2D Materials* **2018**, *5*, 025003.
7. Zhang, J.-Z.; Ma, J.-Z. Two-dimensional excitons in monolayer transition metal dichalcogenides from radial equation and variational calculations. *Journal of Physics: Condensed Matter* **2019**, *31*, 105702.
8. Novoselov, K. S.; Mishchenko, A.; Carvalho, A.; Castro Neto, A. H. 2D materials and van der Waals heterostructures. *Science* **2016**, *353*.
9. Zollner, K.; Faria Junior, P. E.; Fabian, J. Proximity exchange effects in MoSe₂ and

- WSe₂ heterostructures with CrI₃: Twist angle, layer, and gate dependence. *Phys. Rev. B* **2019**, *100*, 085128.
10. Xiang, R.; Inoue, T.; Zheng, Y.; Kumamoto, A.; Qian, Y.; Sato, Y.; Liu, M.; Gokhale, D.; Guo, J.; Hisama, K. *et al.* One-dimensional van der Waals heterostructures. *Science* **2020**, *367*, 537–542.
 11. Gong, L.; Wang, L.; Lu, J.; Han, C.; Chen, W.; Sow, C. H. Photocurrent Response in Multiwalled Carbon Nanotube CoreMolybdenum Disulfide Shell Heterostructures. *The Journal of Physical Chemistry C* **2015**, *119*, 24588–24596.
 12. Artyukhov, V. I.; Gupta, S.; Kutana, A.; Yakobson, B. I. Flexoelectricity and charge separation in carbon nanotubes. *Nano Letters* **2020**, acs.nanolett.9b05345.
 13. Lee, C. H.; Wang, J.; Kayatsha, V. K.; Huang, J. Y.; Yap, Y. K. Effective growth of boron nitride nanotubes by thermal chemical vapor deposition. *Nanotechnology* **2008**, *19*, 455605.
 14. Beal, A. R.; Knights, J. C.; Liang, W. Y. Transmission spectra of some transition metal dichalcogenides. I. Group IVA: Octahedral coordination. *Journal of Physics C: Solid State Physics* **1972**, *5*, 3531–3539.
 15. Aleithan, S. H.; Livshits, M. Y.; Khadka, S.; Rack, J. J.; Kordesch, M. E.; Stinaff, E. Broadband femtosecond transient absorption spectroscopy for a CVD MoS₂ monolayer. *Physical Review B* **2016**, *94*, 035445.
 16. Qiu, D. Y.; da Jornada, F. H.; Louie, S. G. Optical Spectrum of MoS₂: Many-Body Effects and Diversity of Exciton States. *Phys. Rev. Lett.* **2013**, *111*, 216805.
 17. Nguyen, P. V.; Teutsch, N. C.; Wilson, N. R. N. P.; Kahn, J.; Xia, X.; Graham, A. J.; Kandyba, V.; Giampietri, A.; Barinov, A.; Constantinescu, G. C. *et al.* Visualizing

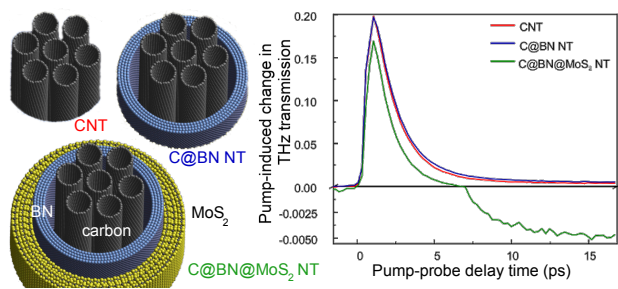
- electrostatic gating effects in two-dimensional heterostructures. *Nature* **2019**, *572*, 220–223.
18. Pogna, E. A. A.; Marsili, M.; De Fazio, D.; Dal Conte, S.; Manzoni, C.; Sangalli, D.; Yoon, D.; Lombardo, A.; Ferrari, A. C.; Marini, A. *et al.* Photo-induced bandgap renormalization governs the ultrafast response of single-layer MoS₂. *ACS Nano* **2016**, *10*, 1182–1188.
 19. Milošević, I.; Nikolić, B. c. v.; Dobardžić, E.; Damnjanović, M.; Popov, I.; Seifert, G. Electronic properties and optical spectra of MoS₂ and WS₂ nanotubes. *Phys. Rev. B* **2007**, *76*, 233414.
 20. Zhang, Q.; Hároz, E. H.; Jin, Z.; Ren, L.; Wang, X.; Arvidson, R. S.; Lüttge, A.; Kono, J. Plasmonic nature of the terahertz conductivity peak in single-wall carbon nanotubes. *Nano Letters* **2013**, *13*, 5991–5996.
 21. Shao, D.; Yotprayoonsak, P.; Saunajoki, V.; Ahlskog, M.; Virtanen, J.; Kangas, V.; Volodin, A.; Haesendonck, C. V.; Burdanova, M.; Mosley, C. D. *et al.* Conduction properties of thin films from a water soluble carbon nanotube/hemicellulose complex. *Nanotechnology* **2018**, *29*, 145203.
 22. Burdanova, M. G.; Tsapenko, A. P.; Satco, D. A.; Kashtiban, R.; Mosley, C. D. W.; Monti, M.; Staniforth, M.; Sloan, J.; Gladush, Y. G.; Nasibulin, A. G. *et al.* Giant negative terahertz photoconductivity in controllably doped carbon nanotube networks. *ACS Photonics* **2019**, *6*, 1058–1066.
 23. Britnell, L.; Gorbachev, R. V.; Jalil, R.; Belle, B. D.; Schedin, F.; Katsnelson, M. I.; Eaves, L.; Morozov, S. V.; Mayorov, A. S.; Peres, N. M. R. *et al.* Electron tunneling through ultrathin boron nitride crystalline barriers. *Nano Letters* **2012**, *12*, 1707–1710.
 24. Shen, C.-C.; Hsu, Y.-T.; Li, L.-J.; Liu, H.-L. Charge dynamics and electronic structures

- of monolayer MoS₂ films grown by chemical vapor deposition. *Applied Physics Express* **2013**, *6*, 125801.
25. Lee, C.; Yan, H.; Brus, L. E.; Heinz, T. F.; Hone, J.; Ryu, S. Anomalous lattice vibrations of single- and few-Layer MoS₂. *ACS Nano* **2010**, *4*, 2695–2700.
26. Molina-Sánchez, A.; Wirtz, L. Phonons in single-layer and few-layer MoS₂ and WS₂. *Phys. Rev. B* **2011**, *84*, 155413.
27. Ghorbani-Asl, M.; Zibouche, N.; Wahiduzzaman, M.; Oliveira, A. F.; Kuc, A.; Heine, T. Electromechanics in MoS₂ and WS₂: Nanotubes vs. monolayers. *Scientific Reports* **2013**, *3*, 2961.
28. Evarestov, R. A.; Bandura, A. V. Infrared and Raman active vibrational modes in MoS₂-based nanotubes: Symmetry analysis and first-principles calculations. *Journal of Computational Chemistry* **2018**, *39*, 2163–2172.
29. Carvalho, B. R.; Wang, Y.; Mignuzzi, S.; Roy, D.; Terrones, M.; Fantini, C.; Crespi, V. H.; Malard, L. M.; Pimenta, M. A. Intervalley scattering by acoustic phonons in two-dimensional MoS₂ revealed by double-resonance Raman spectroscopy. *Nature Communications* **2017**, *8*, 14670.
30. Gontijo, R. N.; Resende, G. C.; Fantini, C.; Carvalho, B. R. Double resonance Raman scattering process in 2D materials. *Journal of Materials Research* **2019**, *34*, 1976 – 1992.
31. Gladush, Y.; Mkrtchyan, A. A.; Kopylova, D. S.; Ivanenko, A.; Nyushkov, B.; Kobtsev, S.; Kokhanovskiy, A.; Khagai, A.; Melkumov, M.; Burdanova, M. *et al.* Ionic liquid gated carbon nanotube saturable absorber for switchable pulse generation. *Nano Letters* **2019**, *9*, 5836–5843.
32. Chernikov, A.; Ruppert, C.; Hill, H. M.; Rigosi, A. F.; Heinz, T. F. Population inversion

- and giant bandgap renormalization in atomically thin WS₂ layers. *Nature Photonics* **2015**, *9*, 466–470.
33. Ulbricht, R.; Hendry, E.; Shan, J.; Heinz, T. F.; Bonn, M. Carrier Dynamics in Semiconductors Studied With Time-Resolved Terahertz Spectroscopy. *Reviews of Modern Physics* **2011**, *83*, 543–586.
 34. Lloyd-Hughes, J.; Jeon, T. I. A Review of the Terahertz Conductivity of Bulk and Nanomaterials. *Journal of Infrared, Millimeter, and Terahertz Waves* **2012**, *33*, 871–925.
 35. Docherty, C. J.; Stranks, S. D.; Habisreutinger, S. N.; Joyce, H. J.; Herz, L. M.; Nicholas, R. J.; Johnston, M. B. An ultrafast carbon nanotube terahertz polarisation modulator. *Journal of Applied Physics* **2014**, *115*, 203108.
 36. Lui, C. H.; Frenzel, A. J.; Pilon, D. V.; Lee, Y.-H.; Ling, X.; Akselrod, G. M.; Kong, J.; Gedik, N. Trion-induced negative photoconductivity in monolayer MoS₂. *Phys. Rev. Lett.* **2014**, *113*, 166801.
 37. Xing, X.; Zhao, L.; Zhang, Z.; Lin, X.; Yu, Y.; Jin, Z.; Liu, W.; Zhang, W.; Ma, G. The modulation of terahertz photoconductivity in CVD grown n-doped monolayer MoS₂ with gas adsorption. *Journal of Physics: Condensed Matter* **2019**, *31*, 245001.
 38. Cha, S.; Sung, J. H.; Sim, S.; Park, J.; Heo, H.; Jo, M.-H.; Choi, H. 1s-intraexcitonic dynamics in monolayer MoS₂ probed by ultrafast mid-infrared spectroscopy. *Nature Communications* **2016**, *7*, 10768.
 39. Radisavljevic, B.; Radenovic, A.; Brivio, J.; Giacometti, V.; Kis, A. Single-layer MoS₂ transistors. *Nature Nanotechnology* **2011**, *6*, 147–150.
 40. Strait, J. H.; Nene, P.; Rana, F. High intrinsic mobility and ultrafast carrier dynamics in multilayer metal-dichalcogenide MoS₂. *Physical Review B* **2014**, *90*, 245402.

41. Fathipour, S.; Remskar, M.; Varlec, A.; Ajoy, A.; Yan, R.; Vishwanath, S.; Rouvimov, S.; Hwang, W. S.; Xing, H. G.; Jena, D. *et al.* Synthesized multiwall MoS₂ nanotube and nanoribbon field-effect transistors. *Applied Physics Letters* **2015**, *106*, 022114.
42. Docherty, C. J.; Parkinson, P.; Joyce, H. J.; Chiu, M.-H.; Chen, C.-H.; Lee, M.-Y.; Li, L.-J.; Herz, L. M.; Johnston, M. B. Ultrafast Transient Terahertz Conductivity of Monolayer MoS₂ and WSe₂ Grown by Chemical Vapor Deposition. *ACS Nano* **2014**, *8*, 11147–11153.
43. Sun, D.; Rao, Y.; Reider, G. A.; Chen, G.; You, Y.; Brzin, L.; Harutyunyan, A. R.; Heinz, T. F. Observation of rapid exciton - exciton annihilation in monolayer molybdenum disulfide. *Nano Letters* **2014**, *14*, 5625–5629.
44. Wang, H.; Zhang, C.; Rana, F. Ultrafast Dynamics of Defect-Assisted ElectronHole Recombination in Monolayer MoS₂. *Nano Letters* **2015**, *15*, 339–345.
45. Selig, M.; Berghäuser, G.; Raja, A.; Nagler, P.; Schüller, C.; Heinz, T. F.; Korn, T.; Chernikov, A.; Malic, E.; Knorr, A. Excitonic linewidth and coherence lifetime in monolayer transition metal dichalcogenides. *Nature Communications* **2016**, *7*, 13279.

For table of contents only:



Supporting Information for:

Ultrafast optoelectronic processes in 1D radial van der Waals heterostructures: carbon, boron nitride and MoS₂ nanotubes with coexisting excitons and highly mobile charges

Maria G. Burdanova,[†] Reza J. Kashtiban,[†] Yongjia Zheng,[‡] Rong Xiang,[‡]
Chiashi Shohe,[‡] Jack Matthew Woolley,[¶] Michael Staniforth,[¶] Emily
Sakamoto-Rablah,[†] Xue Xia,[†] Matthew A. Broome,[†] Jeremy Sloan,[†] Anton
Anisimov,[§] Esko I. Kauppinen,^{||} Shigeo Maruyama,[‡] and James Lloyd-Hughes^{*,†}

[†]*University of Warwick, Department of Physics, Gibbet Hill Road, Coventry, CV4 7AL, United Kingdom.*

[‡]*Departure of Mechanical Engineering, The University of Tokyo, Tokyo 113-8656, Japan.*

[¶]*University of Warwick, Department of Chemistry, Gibbet Hill Road, Coventry, CV4 7AL, United Kingdom.*

[§]*Canatu Ltd., Vantaa FI-01720, Finland.*

^{||}*Department of Applied Physics, Aalto University School of Science, Espoo 15100, FI-00076 Aalto, Finland.*

E-mail: j.lloyd-hughes@warwick.ac.uk

Methods

Single-walled CNTs were synthesised via the floating-catalyst aerosol CVD method,¹ creating 20 nm-thick films with a network comprising 10% individual and 90% bundled nanotubes (around 5 per bundle). A mean diameter of 2.1 nm was determined from transmission electron microscopy (TEM) of a number of individual tubes, while tube lengths were above 10 μm . As-deposited films were used in order to avoid additional processing steps (such as sonication and surfactant wrapping) which can introduce additional defects, change the chemical and dielectric environment, and reduce the length of the as-grown CNTs. Hence, the films contained a mix of one-third of metallic and two-thirds of semiconducting SWCNTs with a mix of chiralities. Free-standing films were obtained by a dry-transfer technique,² and were used as a matrix for BN and MoS₂ NT growth by CVD.³ The pristine CNT film was preheated at 1050 °C

in Ar/H₂ for 1 hour at low pressure and coated by BNNTs at 1050 °C (1-3 hr) at low pressure, and subsequently cooled slowly to room temperature. The MoS₂ growth was performed at 550 °C at low pressure, and also cooled slowly to room temperature. As-grown the outer BNNT and MoS₂ were evenly distributed in chirality.³ After optical characterisation films were transferred to TEM grids for electron microscopy characterisation.

The equilibrium absorbance spectra were obtained by Lambda 1050 UV/vis/IR spectrophotometer (200-1200 THz range; 250-1500 nm wavelength), Bruker Vertex 70V IR and Perkin Elmer Spectrum GX Fourier-transform infrared spectrometers (3-200 THz) and a home-made THz time-domain spectrometer (0.12-4 THz). Raman spectra were obtained using a confocal microspectrometer (Labram, Jobin-Yvon Horiba) with 660 nm and 488 nm lasers (spectral resolution 0.5 cm^{-1}) and Renishaw inVia

Reflex Raman Microscopes with 442 nm and 532 nm lasers.

The optical pump beam in OPTP and transient absorption spectroscopy were created by an optical parametric amplifier (TOPAS), seeded with a 1 kHz, 40 fs, 800 nm pulse (from a Newport Spectra Physics Spitfire Ace) to create pulses with a tunable centre wavelength. The OPTP spectrometer used has been described previously.⁴ For the visible probe, a white-light supercontinuum was generated by focusing the attenuated 800 nm fundamental beam into a vertically translated 2 mm-thick CaF₂ window. Changes in absorbance created by the pump pulse (500 Hz modulation frequency) were measured through the change in transmitted probe intensity, using a fibre-coupled spectrometer. The transient absorption was chirp-corrected using the KOALA package.⁵ Transient absorption data were obtained in transmission mode, ignoring reflection and scattering, and thus slightly overestimated the absorption. The absorption spectra at different pump-probe delay times were fit to a model with four Gaussian peaks and a broad background represented by a straight line. The linear background contribution was constant for all fits and accounts for absorption processes including the CNTs' π -plasmon and the MoS₂ NTs' interband absorption.

References

1. Nasibulin, A. G.; Moisala, A.; Brown, D. P.; Jiang, H.; Kauppinen, E. I. A novel aerosol method for single walled carbon nanotube synthesis. *Chemical Physics Letters* **2005**, *402*, 227–232.
2. Nasibulin, A. G.; Kaskela, A.; Mustonen, K.; Anisimov, A. S.; Ruiz, V.; Kivist, S.; Rackauskas, S.; Timmermans, M. Y.; Pudas, M.; Aitchison, B. *et al.* Multifunctional free-standing single-walled carbon nanotube films. *ACS Nano* **2011**, *5*, 3214–3221.
3. Xiang, R.; Inoue, T.; Zheng, Y.; Kumamoto, A.; Qian, Y.; Sato, Y.; Liu, M.; Gokhale, D.; Guo, J.; Hisama, K. *et al.* One-dimensional van der Waals heterostructures. *Science* **2020**, *367*, 537–542.
4. Monti, M.; Tao, S. X.; Staniforth, M.; Crocker, A.; Griffin, E.; Wijesekara, A.; Hatton, R. A.; Lloyd-Hughes, J. Efficient In-traband Hot Carrier Relaxation in the Perovskite Semiconductor Cs_{1-x}Rb_xSnI₃ Mediated by Strong Electron-Phonon Coupling. *Journal of Physical Chemistry C* **2018**, *122*, 20669–20675.
5. Grubb, M. P.; Orr-Ewing, A. J.; Ashfold, M. N. R. KOALA: A program for the processing and decomposition of transient spectra. *Review of Scientific Instruments* **2014**, *85*, 064104.

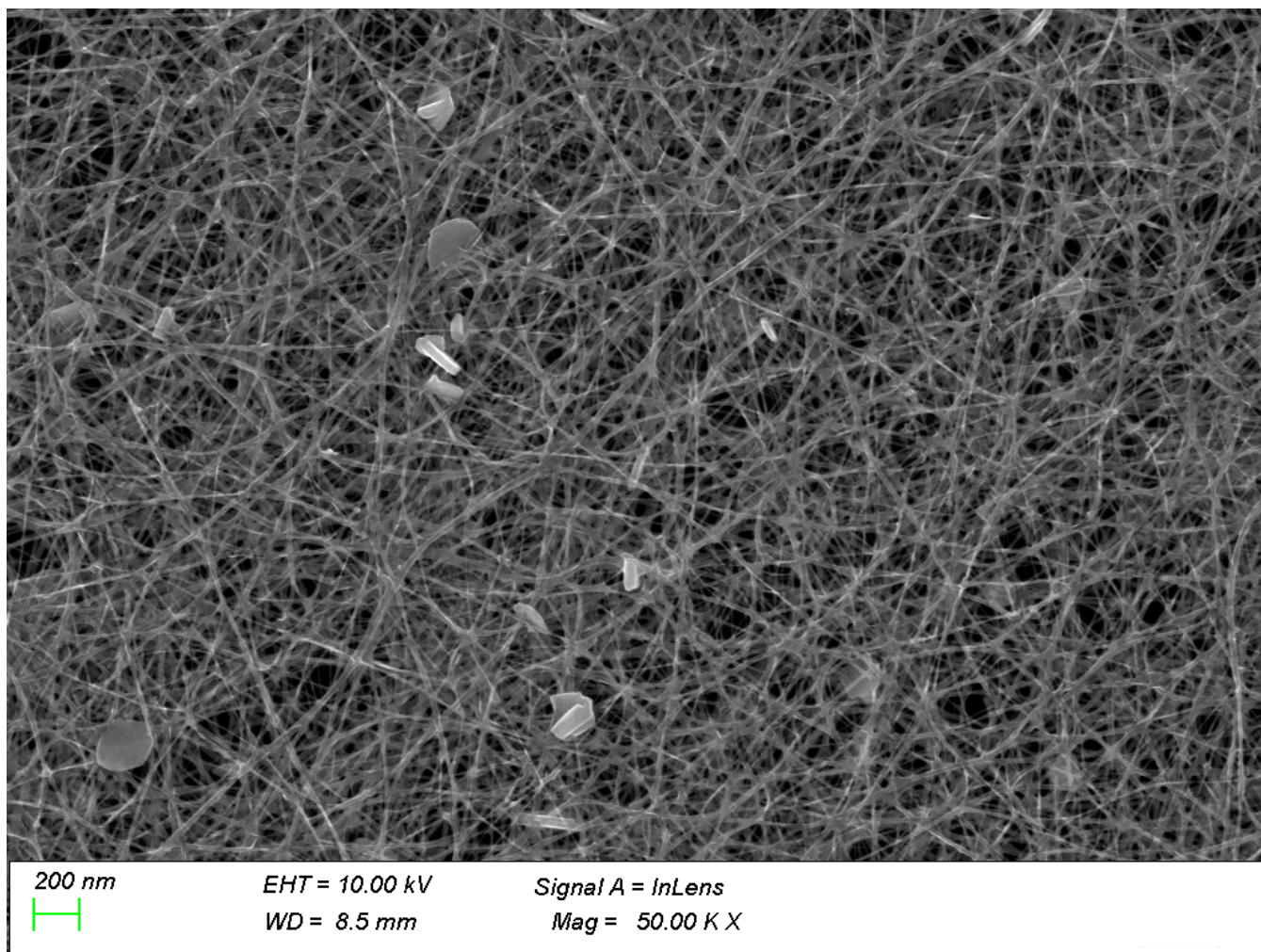


Figure S1: Low magnification scanning electron micrograph of a C@BN@MoS₂ film. The majority of the free-standing film consists of long MoS₂ nanotubes, outside BN nanotubes and CNT bundles. A small fraction (< 2 %) of MoS₂ nanoparticles are also evident.

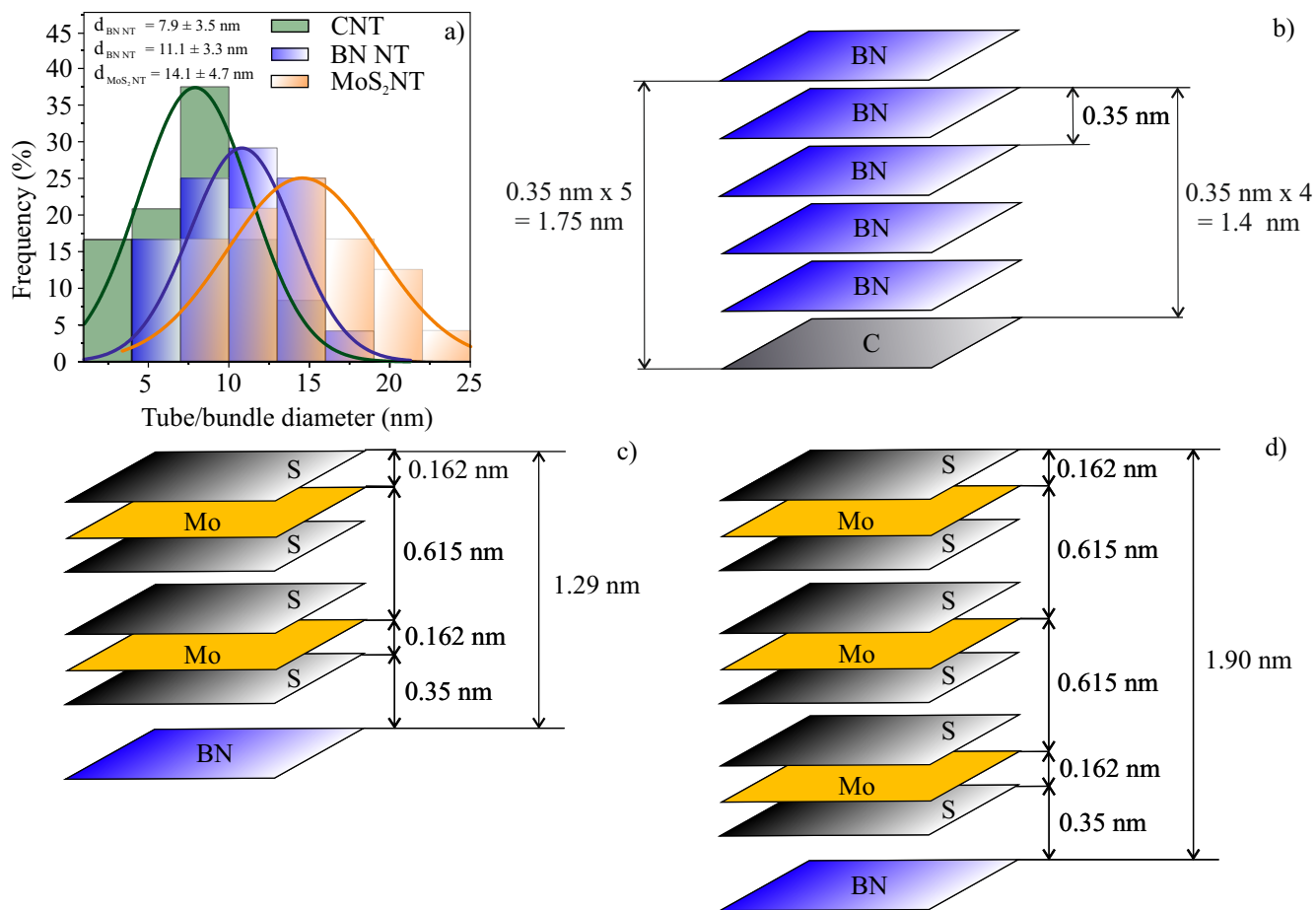


Figure S2: Analysis of the diameters and thickness of the walls. Fig. S2(a) shows the diameter distribution of the C@BN NT (blue) and MoS₂ (orange) NTs and CNT bundles (green) based on TEM observations. The sequential growth of the BN on CNT and then MoS₂ on the BN@CNT increases the mean diameter d without altering the width substantially. A similar variance for the CNT, BNNT and MoS₂ NT diameter distributions indicated relatively uniform BN and MoS₂ layer thicknesses. (b)-(d) The interlayer spacing and thickness of each compound in the vdW heterostructure is shown schematically. For (b) the total thickness of 4-5 BN layers in the C@BN NT heterostructure adds an additional 1.4 nm-1.75 nm on each side of the CNT or CNT bundle, accounting for the increase in mean d seen in (a) from the CNT to C@BN NT sample. Similarly, (c) and (d) show the total thickness of two or three MoS₂ layers in the C@BN@MoS₂ NT heterostructure: two monolayers will add 2.6 nm to the composite's external diameter, while three monolayers will add 3.8 nm. The extra diameter experimentally (panel (a)) is 3.0 nm.

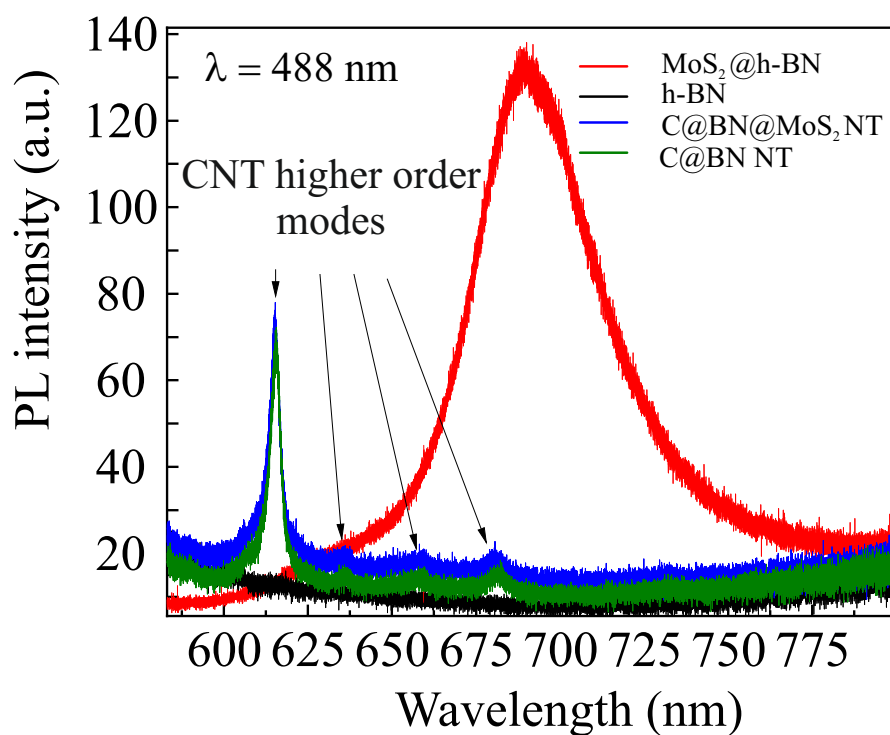


Figure S3: Photoluminescence of MoS₂ - based nanostructures. Photoluminescence spectra of a 2D monolayer MoS₂ on h-BN (red), h-BN (black), C@BN@MoS₂ (blue) and C@BN NT (green) measured in the spectral range of the A and B excitons at room temperature under 488 nm excitation. While the monolayer 2D MoS₂ exhibited photoluminescence, the 1D-C@BN@MoS₂ heterostructure didn't show any emission in the same spectral range.

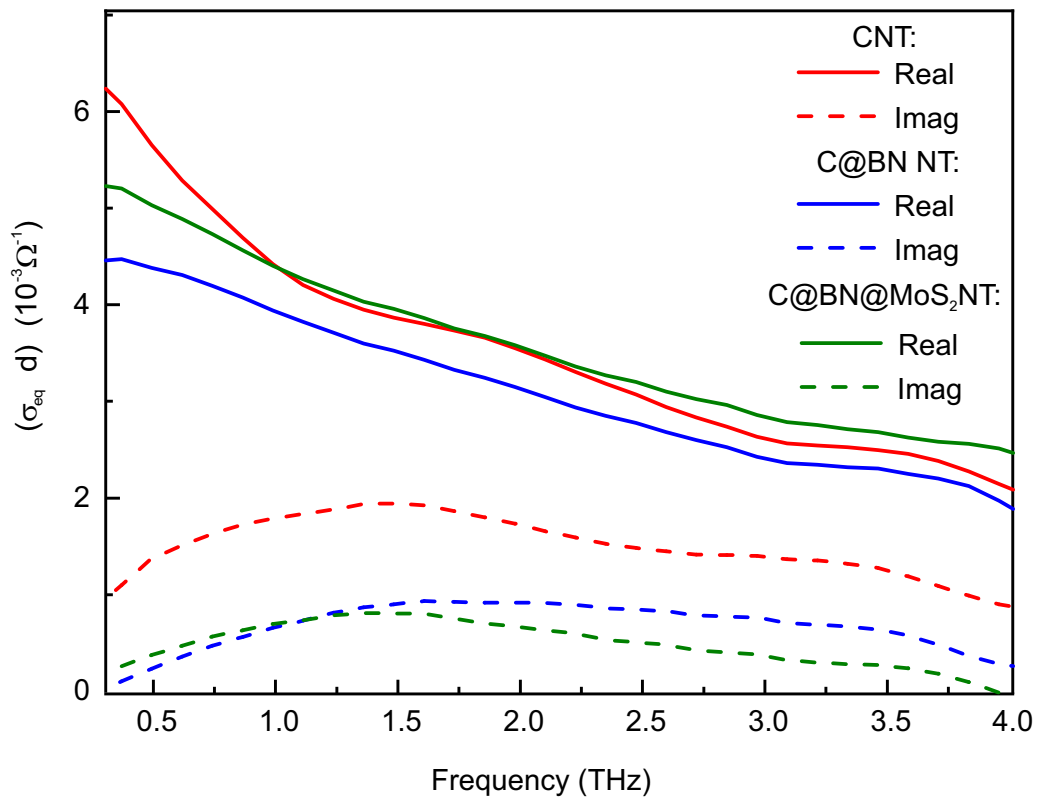


Figure S4: Real (solid lines) and imaginary (dash lines) of equilibrium conductivity of C (red), C@BN (blue) and C@BN@MoS₂(green) NT films

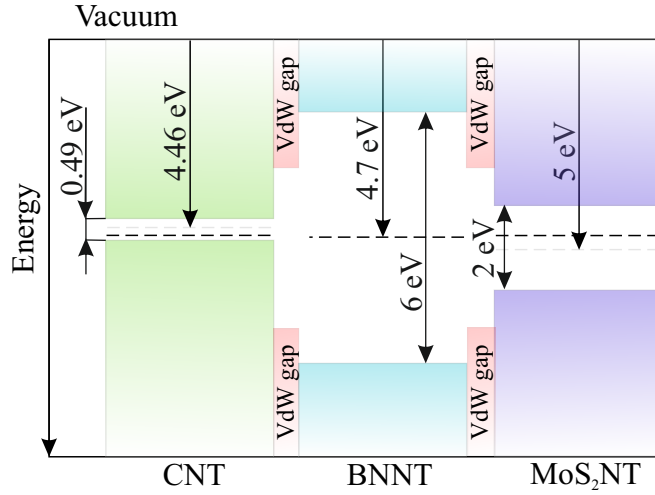


Figure S5: Estimated band alignment in the C@BN@MoS₂ heterostructure. The work function of SWCNT is about 4.46 eV [Su et al., Phys. Rev. B 76 235413 (2007)] while the electron affinity of h-BN is around 2 eV [Sup Choi et al., Nature Communications 4 1624 (2013)]. The work function of monolayer MoS₂ is about 5 eV [Gong et al., Appl. Phys. Lett. 103 053513 (2013)]. For 2.1 nm carbon nanotubes the direct band gap between the first van Hove singularities of semiconducting nanotubes is about 0.46 eV while for MoS₂ it is about 2 eV. Green, cyan and violet represent the bands in CNTs BNNTs and MoS₂. The dashed lines show the position of the Fermi level. The high energetic barrier created by the BN prohibits rapid electron or hole transfer from the MoS₂ to the CNTs.

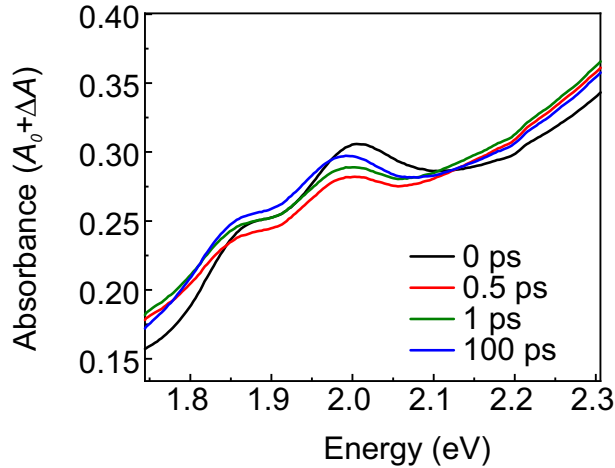


Figure S6: Transient absorption spectroscopy of C@BN@MoS₂ NT film at A and B excitons peak positions. Transient absorption spectra, $A(E, t) = A_0(E) + \Delta A(E, t)$, as a function of pump-probe delay time t and probe beam energy E (excitation wavelength 350 nm; 1 mJcm⁻² fluence). Data (solid colored lines) are shown at $t = 0.0$ ps, $t = 0.5$ ps, $t = 1$ ps and $t = 100$ ps. Here, $t = 0.0$ ps was defined as the probe pulse arriving just before the pump pulse, and hence shows the equilibrium absorbance.

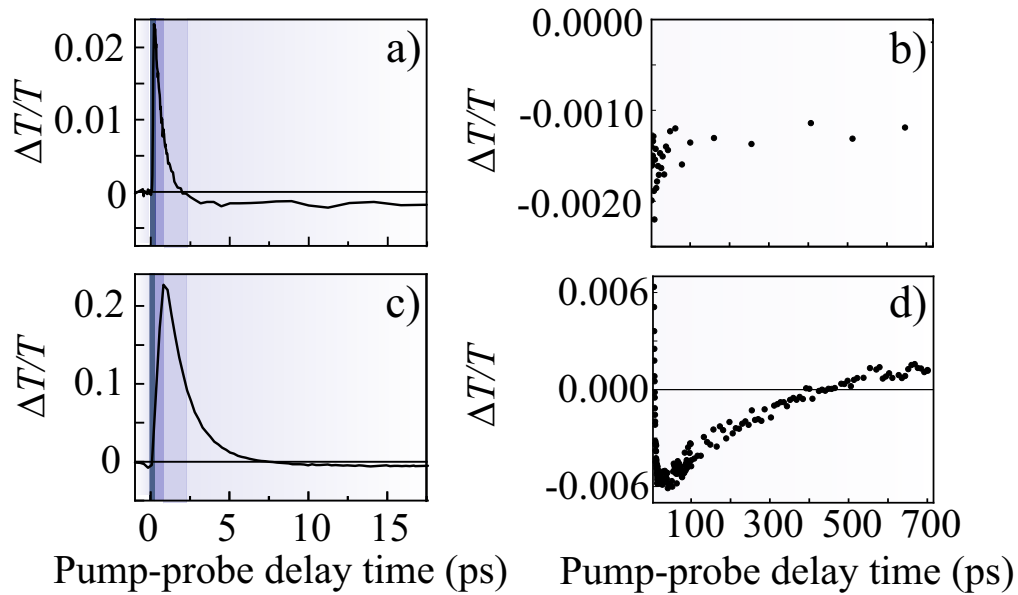


Figure S7: Comparison of ultrafast optical probe and THz probe spectroscopy. Data are shown for the C@BN@MoS₂ NTs at 435 nm pump wavelength at 0.2 mJ/cm² fluence. Optical pump, optical probe (wavelength 435 nm) data ($\Delta T/T$ denotes the change in intensity of the probe) at earlier (a) and later (b) time delays; (c) and (d) show the transient THz response ($\Delta T/T$ denotes the differential THz electric field) at earlier and later pump-probe delays. Note that the optical probe examines the change in exciton absorption strength, where negative $\Delta T/T$ shows an increase in absorption, and this does not recover after 1 ns, indicating that excitons persist over this time window. In contrast, the THz probe shows a negative $\Delta T/T$ that reduces over the same time window and tends to the positive $\Delta T/T$ seen for CNTs, indicating the recombination time for free charges in MoS₂ is faster than the exciton lifetime.

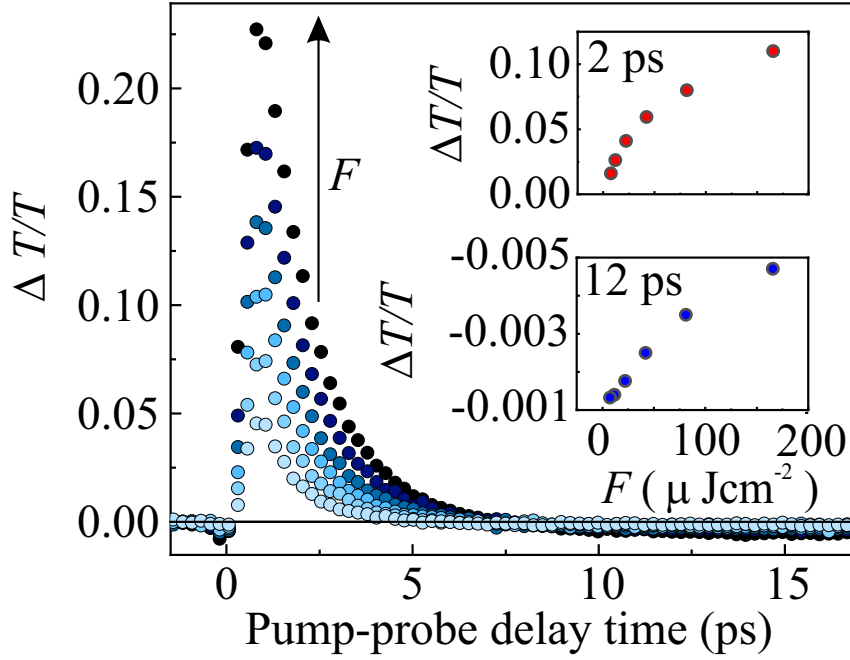


Figure S8: Fluence dependence of differential THz transmission, $\Delta T/T$, for C@BN@MoS₂ heterostructure. Transient THz response at 435 nm pump wavelength with fluence $F = 0 - 0.2 \text{ mJ}/\text{cm}^2$. The insets show how $\Delta T/T$ varies with fluence at fixed pump-probe delays of 2 ps (top inset) and 12 ps (bottom inset). A negative $\Delta T/T$ is evident at later times for all fluences.